Growth and shape of a laboratory alluvial fan

Pauline Delorme, O. Devauchelle, L. Barrier, F. Métivier

Growth and shape of a laboratory alluvial fan

P. Delorme, O. Devauchelle,* L. Barrier, and F. Métivier
Institut de Physique du Globe de Paris, Sorbonne Paris Cité, Université Paris Diderot, CNRS, UMR7154, 1 rue Jussieu, 75238 Paris Cedex 05, France

(Received 9 March 2018; published xxxxxx)

Using laboratory experiments, we investigate the influence of water and sediment discharges on the morphology of an alluvial fan. In our flume, a single-thread laminar river deposits corundum sand into a conical fan. We record the fan progradation with top-view images and measure its shape using the deformation of a Moiré pattern. The fan remains virtually self-affine as it grows, with a nearly constant slope. We find that, when the sediment discharge is small, the longitudinal slope of the fan remains close to that of a river at the threshold for sediment transport. Consequently the slope depends on the water discharge only. A higher sediment discharge causes the fan's slope to depart from the threshold value. Due to the downstream decrease of the sediment load, this slope gets shallower towards the fan's toe. This mechanism generates a concave fan profile. This suggests that we could infer the sediment flux that feeds a fan based on its proximal slope.

DOI: 10.1103/PhysRevE.00.002900

I. INTRODUCTION

Alluvial fans are sedimentary deposits which form at the outlet of mountain ranges. When a river flows through a mountain range, the flow-induced shear stress entrains sediment particles and carries them downstream. As it reaches the plain, the river loses its lateral confinement, and its slope drops. These changes induce sediment deposition [1–5]. As the river deposits its load, its bed rises until it overflows to find a new path. This phenomenon, called avulsion, maintains the radial symmetry of the deposit through time [6–8]. The geometry of the fan thus depends on the conditions under which it was built.

Three parameters are known to control the slope of an alluvial fan: the water discharge Q_w, the sediment discharge Q_s, and the sediment size d_s [9]. Field observations show that, in most cases, the slope of the fan increases with d_s and Q_s, whereas it decreases with Q_w [10–12]. There is no consensus yet about the physical origin of these relations or about their mathematical formulation [12].

Analogues of alluvial fans are easily produced in the laboratory, and they accord qualitatively with field observations [13–16]. Most authors represent the slope as a function of the discharge ratio Q_s/Q_w and find a positive correlation [17–21]. This function, however, appears to vary from experiment to experiment, suggesting that we investigate the influence of the water and the sediment discharges independently [20].

Guerit *et al.* [22] have produced an alluvial fan confined between two plexiglass plates. This experimental setup dictates the width of the river and precludes avulsion, thus simplifying the interpretation of the results. When the sediment discharge is vanishingly small, the fan adjusts its shape to keep the river's bed near the threshold of motion. Its profile is then virtually linear, and its slope depends only on water discharge and sediment size. To the contrary, a finite sediment load affects the fan's shape—it steepens with sediment discharge. As sediment gets deposited along the fan, the slope shallows downstream, resulting in a concave upward profile [12,22].

Building upon this study, we remove the plexiglass plates that confine the flow and build a complete fan with a more realistic geometry. By doing so, we allow the river to (1) spontaneously select its own size and slope [23] and (2) distribute sediment over a self-formed lobe [14,24].

We design an experimental setup to generate an alluvial fan fed by a single-thread channel. We first impose a low sediment discharge, to remain near the threshold of sediment motion, and use the work of Seizilles *et al.* [25] to express the slope of our fan as a function of the water discharge (Sec. II). We then increase the sediment discharge to investigate its impact on the fan's profile (Sec. III). Finally, we show that we can infer the water and sediment discharges of a fan from its profile.

II. SINGLE-THREAD LABORATORY FAN

A. Experimental setup

We produce our experimental fan in a 80-cm-wide and 50-cm-long tank. At the back of the tank, a 15-cm-high vertical wall simulates a mountain front. At the center of this wall, a 2.5-cm-wide tilted channel directs the sediment and fluid mixture toward the tank. The opposite side of the tank is bounded by a trench to evacuate the fluid. To prevent any fluid accumulation at the outlet, the fan lies on a 60-cm-wide and 30-cm-long shelf covered with a 200 μm sieve mesh. This setup allows us to build a fan with an opening angle of 180° (Fig. 1).

We use a viscous mixture of water (40 %) and glycerol (60 %) to maintain a laminar flow, at a Reynolds number of about 50 (density $\rho = 1150\ \mathrm{kg\,m^{-3}}$ and viscosity $\nu = 7 \times 10^{-6}\ \mathrm{m^2\,s}$). A header tank provides a constant fluid discharge, which value we monitor using an electromagnetic flowmeter (Kobold, MIK-5NA10AE34R). Water evaporation concentrates the glycerol mixture. We measure its density

*devauchelle@ipgp.fr

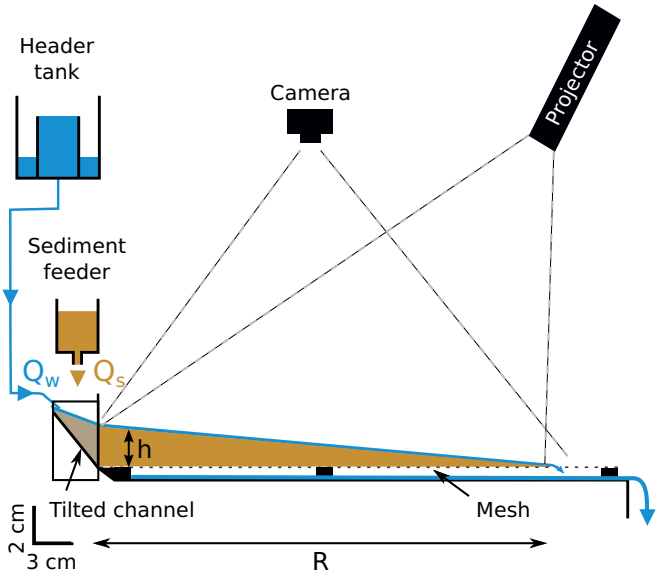

FIG. 1. Experimental setup. Blue: water-glycerol mixture. Gold: corundum sediment. Fluid and sediment discharges are Q_w and Q_s, respectively.

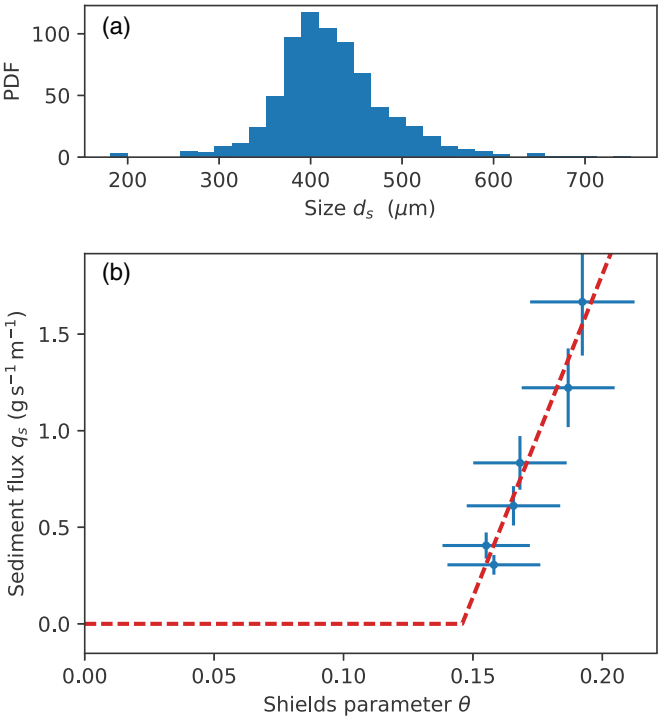

FIG. 2. (a) Sediment-size distribution. (b) Transport law. Blue dots and error bars: measurements. Red dashed line: Eq. (1), with $q_0 = 33.4 \pm 0.7$ g s^{-1} m^{-1} and $\theta_c = 0.14 \pm 0.005$.

twice a day and compensate for evaporation with fresh water. As a result, the fluid discharge varies by less than 5% during an experiment, an indication that the viscosity of the fluid is also reasonably constant.

At the experiment inlet, a tilted channel mixes the fluid with a well-sorted sediment composed of corundum grains (crystalline aluminium oxide). We measure the grain size using image analysis [$d_{50} = 416 \pm 45$ μm; Fig. 2(a)] and its density using a pycnometer ($\rho_s = 3900 \pm 56$ kg m^{-3}). At the macroscopic scale, the physical properties of the grain translate into a friction coefficient ($\mu = 0.7$) and a transport law relating the bedload intensity to the shear stress τ, namely,

$$q_s = q_0(\theta - \theta_c), \tag{1}$$

where $\theta = \tau/[(\rho_s - \rho)gd_s]$ is the Shields parameter with g the acceleration of gravity [26]. We measure the transport law of our corundum sediment with an independent experimental setup [22,27,28]. We find a critical Shields number $\theta_c = 0.14 \pm 0.005$ and a prefactor $q_0 = 33.4 \pm 0.7$ g s^{-1} m^{-1} [Fig. 2(b)].

To produce a single-thread laboratory fan, the sediment discharge has to be low and constant throughout the fan growth. To achieve this, we have designed a conveyor-belt sediment dispenser. Sediments are stored in a hopper placed over a 3.5-cm-wide conveyor belt (Norcan). A stepper motor controlled by an Arduino motor shield drives the belt. To adjust the sediment discharge, we can adjust two parameters: the distance between the hopper and the belt, and the belt speed. To monitor the sediment discharge injected into the experiment, the entire device is placed on an electronic scale (Ohaus, Explorer 35), which measures the weight of the dispenser every minute.

B. Radially symmetric alluvial fan

At the beginning of an experiment, the surface of the experimental setup is bare. We start the fluid and sediment feed at the same time and keep them constant during the entire experimental run. To monitor the fan evolution, we acquire top-view pictures using a camera fixed above the tank center (Canon EOS 100 D with a Canon 28-105 mm $f/3.5$–4.5 APO macro 0.5 m/1.6 ft Ultrasonic lens). We record a picture every 10 min (Fig. 3).

The growth of our fan is similar to the ones of Van Dijk *et al.* [19] and Reitz and Jerolmack [24]. The flow alternates between a single channel and a thin sheet of fluid covering a portion of the fan. In our case, however, the flow gets more and more channelized as the fan grows. The channel migrates either through the gradual erosion of its banks or through floodings and abrupt avulsion. This series of avulsions allows the channel to explore the entire fan surface, thus maintaining its radial symmetry (Fig. 3).

Using the top-view pictures, we measure the evolution of the fan radius. To do so, we develop an algorithm that automatically locates the fan toe. Because the fan color is well defined, we can detect its boundary by applying a threshold. We then measure the average radius of the fan by approximating its boundary by a half circle (red dashed lines on Fig. 3). We find that, typically, the distance from the apex to the boundary varies by less than 5% (Fig. 3). After a transient, which duration depends on the sediment discharge, the fan radius increases like the cubic root of time (Fig. 4). This experimental observation accords with the self-similar evolution of a semiconical deposit for which, based on mass balance, we expect $R \propto (Q_s t)^{1/3}$ [24,28].

Because of its radial symmetry, the fan's shape reduces to its downstream profile. Consequently, to describe the growth and shape of our laboratory fans, we need an accurate measurement of their profiles.

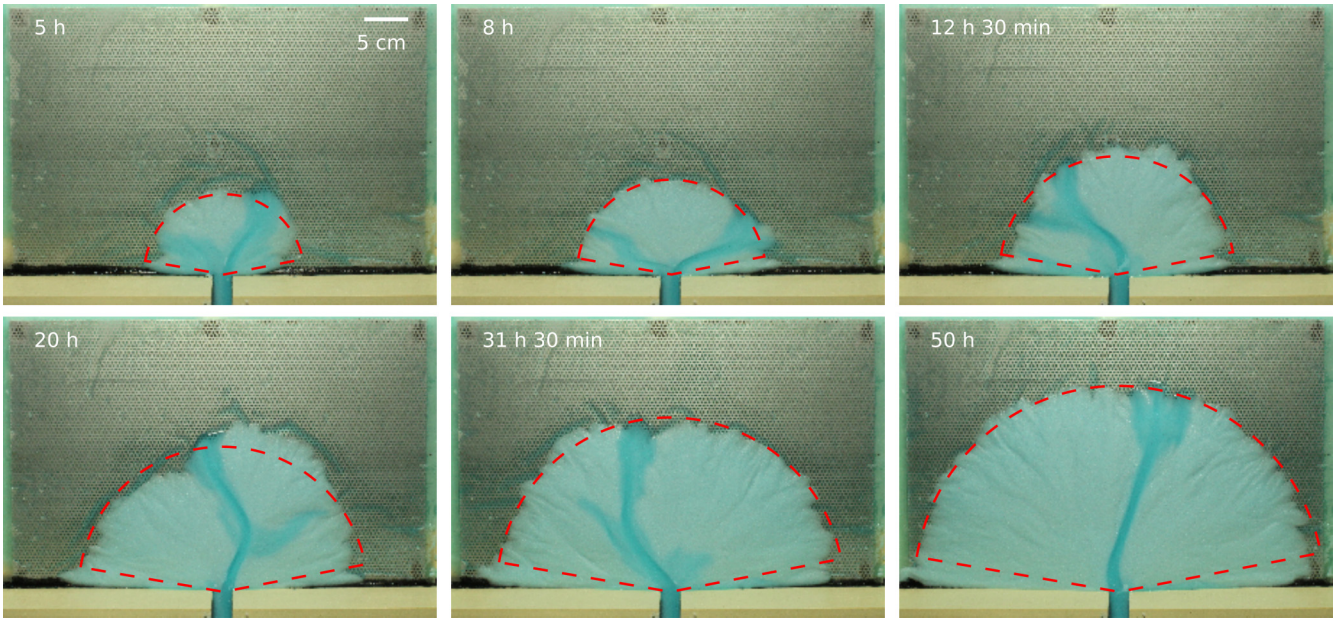

FIG. 3. Top-view pictures of an experimental fan during its growth, run 13 ($Q_w = 0.33\,\mathrm{l\,min^{-1}}$ and $Q_s = 1.68\,\mathrm{g\,min^{-1}}$). Fluid appears in blue, sediment appears in white. Red dashed line indicates the measured radius of the fan.

C. Measurement of the fan elevation

To measure the elevation of our experimental fan, we project a Moiré pattern onto its surface with a video projector [29,30]. We then use the Light3D commercial software to calculate the digital elevation model (DEM) of the deposit [31] (Fig. 5).

To evaluate the accuracy of our measurements, we scan the surface of a tray filled with milk and use it as horizontal reference. We find that the DEM of the milk surface is affected by lens distortion (raw data; Fig. 6). We thus measure the elevation of the milk surface at nine levels ranging from 7 to 134 mm above the bottom of the tank.

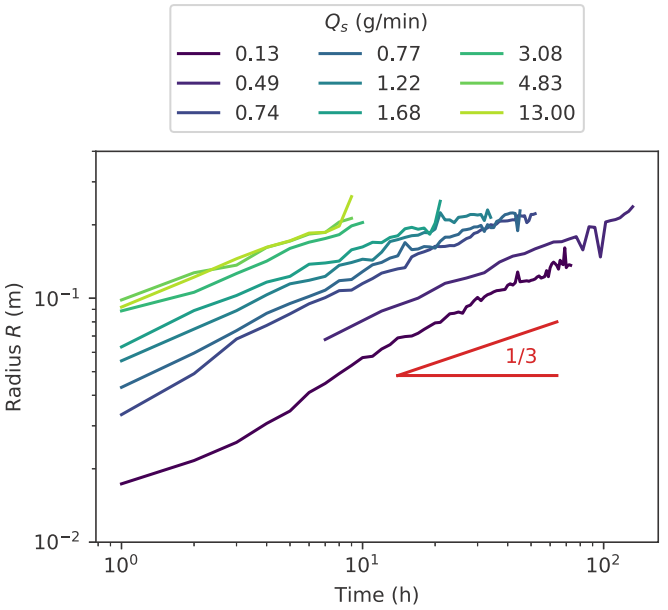

FIG. 4. Evolution of the fan radius ($Q_w = 0.33\,\mathrm{l\,min^{-1}}$, Q_s from 0.13 to 13 $\mathrm{g\,min^{-1}}$).

The lens-induced deformation depends on the coordinates of the pixel and on the distance from the lens (raw data; Fig. 6). We thus fit each DEM of the milk surface with a second-order, two-dimensional polynomial. We then evaluate the six coefficients of this polynomial for each elevation. By applying this correction to the measured DEM of the fan, we reduce the uncertainty of its elevation by a factor of about 10 (Fig. 6). After correction, the uncertainty on the measured elevation is less than 400 μm, which corresponds approximately to the size of a sediment grain.

D. Self-similar growth

The elevation contours of the DEM are well approximated by concentric circles, thus confirming the radial symmetry of the fan (Fig. 5). This property suggests that we can compute the radially averaged profile of the fan with minimal loss of information [24,28] [Fig. 7(a)]. To evaluate how self-similar is the growth of the fan, we normalize its profile by rescaling horizontal and vertical dimensions with its radius, as measured

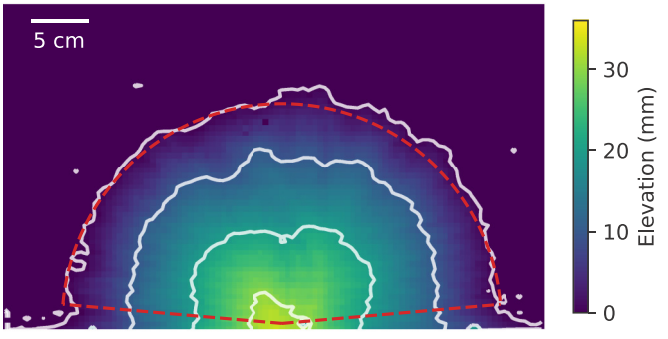

FIG. 5. Digital elevation model (DEM) of an experimental fan (run 13). Contours are 10 mm apart. Red dashed line indicates the measured radius of the fan.

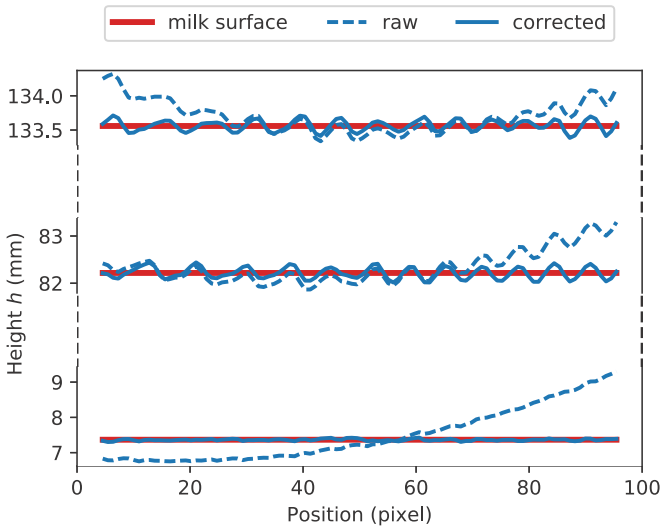

FIG. 6. Profile along the line of maximum deformation of the reference milk surface at different elevations. Dashed blue lines: raw data, solid blue lines: corrected data, red lines: actual elevation of the milk surface.

from the top-view pictures. We find that individual profiles differ from their mean by less than 10 % [Fig. 7(b)].

Based on these observations, we propose to treat the fan's evolution as self-similar. Accordingly, relating the morphology of the fan to the input parameters reduces to understanding how these parameters control its dimensionless profile.

Figure 7 shows that we may approximate the fan profile with a straight line, at least when the sediment discharge is low. We further suggest that the river that feeds the fan controls its slope.

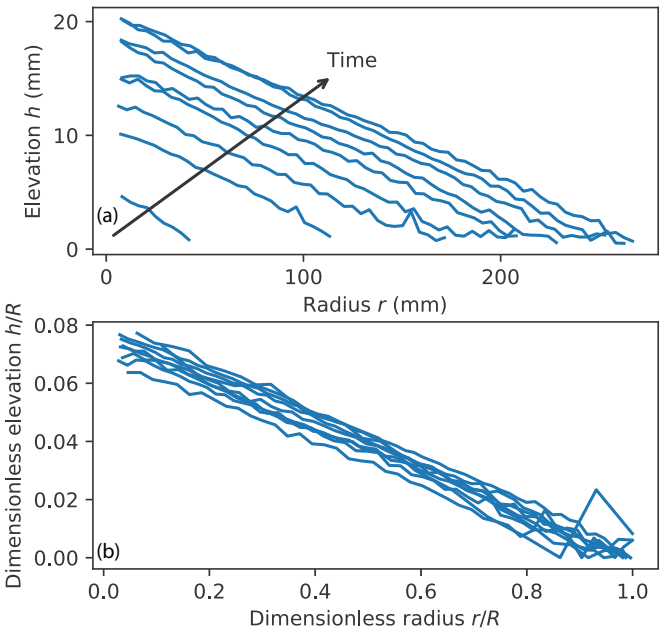

FIG. 7. Radially averaged profiles of an experimental fan (run 4, $Q_w = 0.3\,\mathrm{l\,min^{-1}}$ and $Q_s = 0.2\,\mathrm{g\,min^{-1}}$). (a) Six hours separate two lines. (b) Normalized fan profiles.

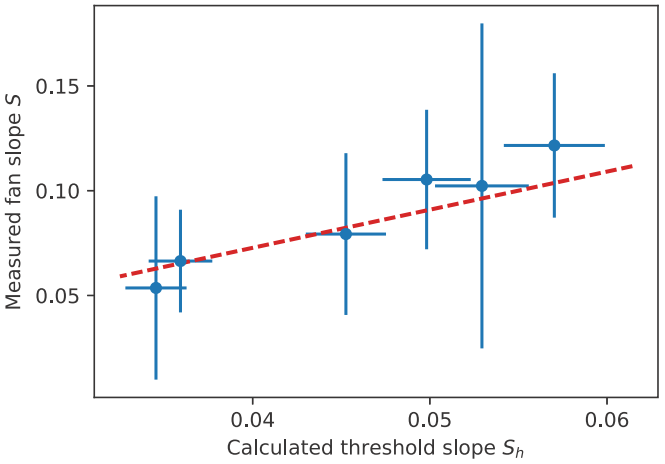

FIG. 8. Slope of the fan as a function of the theoretical threshold slope calculated using Eq. (2) (runs 1 to 6). The red dashed line is a linear fit with slope $A = 1.95$.

In the next section, we test this hypothesis using the work of Seizilles *et al.* [25].

E. Fan near threshold

The shape of an alluvial river results from the mechanical equilibrium of its bed [25,32,33]. When a sediment grain is immersed in a river, two forces act on it: gravity and the flow-induced shear stress. When a river transports a small amount of sediment, we expect its bed to remain near the threshold of sediment motion. At the threshold of motion, the normal component of these forces balances the tangential one. Using this assumption and the shallow-water approximation, Seizilles *et al.* [25] calculated that, for a laminar flow, the threshold slope of a river should read

$$S_h = \mu \left(\frac{4g}{9\nu}\right)^{1/3} \left(\frac{\theta_c}{\mu}\frac{\rho_s - \rho}{\rho} d_s\right)^{4/3} \frac{1}{Q_w^{1/3}}. \qquad (2)$$

We now compare this expression to the slope of our experimental fans. We perform six experiments where the sediment discharge, Q_s, remains fixed at a low value, whereas the fluid discharge, Q_w, varies between experiments (Table I). We then represent the average slope of our experimental fan as a function of the corresponding threshold slope, S_h [Eq. (2)] (Fig. 8). We find that the slope of our experimental fan is proportional to the threshold slope,

$$S = A S_h, \qquad (3)$$

where A is a dimensionless coefficient, whose best-fit value is $A = 1.95 \pm 0.11$. If the shallow-water approximation were perfectly accurate, this coefficient would be one. The value of A we find by fitting our observations, however, depends on the parameters of Eq. (2) and therefore inherits their uncertainty. In Eq. (2) the value of the critical Shields parameter is the least reliable. Although we carefully estimated its value with a dedicated setup [Fig. 2(b)], this measurement remains a matter of debate [34]. Moreover, the critical Shields number is raised to the power 4/3 in Eq. (2). An error on its measurement has therefore a significant impact on the value of the threshold slope S_h.

TABLE I. Experimental parameters for the experimental runs.

Constant sediment discharge		Constant fluid discharge					
$Q_s = 0.2 \pm 0.002$ g min^{-1}		$Q_w = 0.33 \pm 0.02$ l min^{-1}				$Q_w = 0.73 \pm 0.02$ l min^{-1}	
Run	Fluid discharge (l min^{-1})	Run	Sediment discharge (g min^{-1})	Run	Sediment discharge (g min^{-1})	Run	Sediment discharge (g min^{-1})
1	0.9 ± 0.02	7	0.13 ± 0.0084	13	1.68 ± 0.048	18	0.82 ± 0.024
2	0.8 ± 0.02	8	0.49 ± 0.0056	14	3.08 ± 0.12	19	4.9 ± 0.15
3	0.4 ± 0.02	9	0.68 ± 0.013	15	4.83 ± 0.14	20	8.1 ± 0.28
4	0.3 ± 0.02	10	0.74 ± 0.016	16	6.18 ± 0.26		
5	0.25 ± 0.02	11	0.77 ± 0.019	17	13 ± 0.36		
6	0.2 ± 0.02	12	1.22 ± 0.028				

Regardless of the value of A, for a low sediment discharge, we find that the fan's slope remains close to the threshold slope of an alluvial river, indicating that the fan inherits its slope from the river that builds it. We now investigate the influence of the sediment discharge on the fan's profile.

III. DEPARTURE FROM THRESHOLD: INFLUENCE OF SEDIMENT DISCHARGE

A. Sediment transport along the fan

To evaluate the influence of the sediment discharge on the morphology of the fan, we perform 14 additional experiments with different values of Q_s (Table I). We evaluate the error on the sediment discharge by estimating geometrically the volume of sediment deposited in the inlet channel.

The observations of Sec. II B show that the deposit is radially symmetric, thus the spatially averaged profile of the fan suffices to represent its shape. Moreover, the fan grows self-similarly, which allows us to further average the resulting profiles (Sec. II D). To do so, we normalize each profile by dividing its horizontal and vertical coordinates by its radius. Figure 9 shows essentially linear profiles, which steepen with sediment discharge. As the latter vanishes, the fan tends towards a cone at threshold, in accord with Sec. II E.

We now consider the influence of a finite sediment discharge on the fan's slope. Because alluvial fans are depositional systems, only near the apex does the sediment discharge equals the input. Accordingly, we consider only the proximal slope S_p of our fans, where $r/R < 0.4$ (Fig. 9). However, the inlet disturbs the profile, which can be flat or even convex near the apex (Fig. 9). To avoid this disturbance, we measure the proximal slope, S_p, where the dimensionless radius, r/R, lies between 0.1 and 0.4 (proximal area on Fig. 9).

In our experiments, the water discharge takes two values (Table I, run 7 to 20) and so does the associated threshold slope, S_h (Sec. II). To investigate the departure from this threshold slope, we first normalize the proximal slope of our fans with the threshold slope, S_p/S_h. We then represent this dimensionless slope as a function of the dimensionless sediment discharge $Q_s/(q_0 d_s)$, where q_0 is the prefactor of the transport law [Fig. 2(b)] and d_s the sediment size (Fig. 10).

Our observations gather around a single curve the plane defined by the dimensionless sediment discharge and slope, suggesting that normalizing the fan's slope with S_h removes the influence of water discharge. This finding accords with Guerit *et al.* [22], who were also able to separate the influence of water and sediment discharges, although with the different functional form that corresponds to the geometry of their experiment.

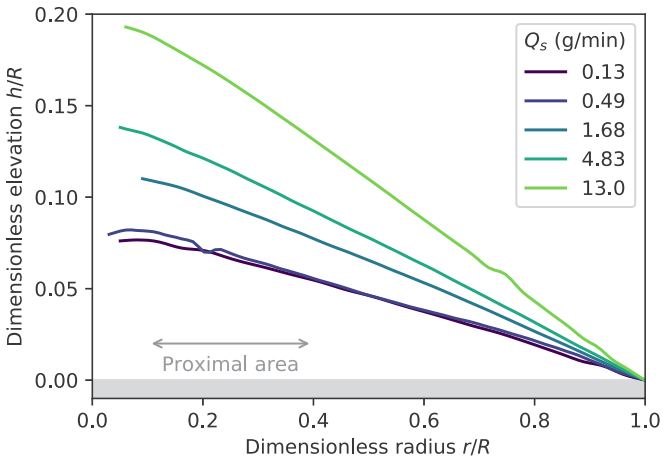

FIG. 9. Normalized fan profiles for five experiments ($Q_w = 0.33$ l min^{-1}, Q_s from 0.13 to 13 g min^{-1}).

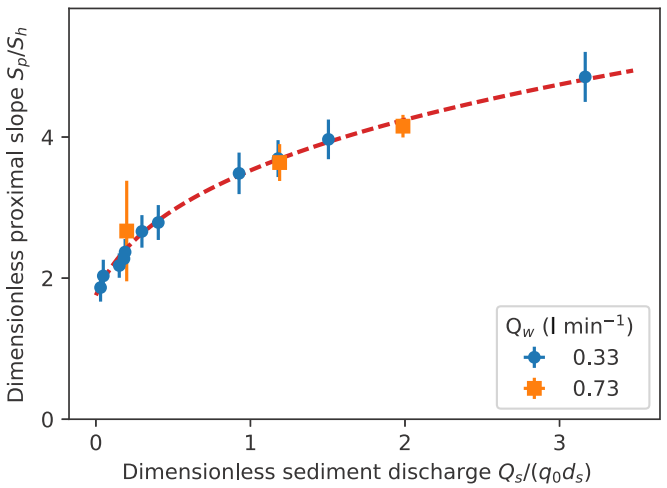

FIG. 10. Normalized proximal slope as a function of the dimensionless sediment discharge. Red dashed line: Eq. (4).

We now propose to fit our experimental data with the following expression:

$$\frac{S}{S_h} = A\left(1 + B\frac{Q_s}{q_0\, d_s}\right)^{\alpha}, \tag{4}$$

where B and α are dimensionless coefficients which we need to fit to our data. By definition, A is the ratio of the measured threshold slope to the theoretical threshold slope [Eq. (3)]. A least-mean-square fit of the three parameters yields $A = 1.85 \pm 0.19$, $B = 0.18 \pm 0.09$, and $\alpha = 0.32 \pm 0.02$. This value of A is close to the one of Sec. II E (Figs. 8 and 10).

Based on Eq. (4), we can now define rigorously what "a small sediment discharge" means. When $Q_s/(q_0\, d_s)$ is much smaller than one, the influence of the sediment discharge on the fan profile is negligible. We then recover the threshold slope defined in Sec. II E.

Equation (4) formulates sediment transport at the scale the river [as opposed to the local transport law of Fig. 2(b)]. It is a function of the river's slope, and therefore of the fan's, which results from the internal equilibrium of the river. We now inject this empirical transport law into the sediment mass balance to calculate the fan profile.

B. Fan profile

The fan grows from sediment deposition, a process formalized by mass balance, which is often referred to as the "Exner equation" in the context of sediment transport [35]:

$$\rho_s(1-\lambda)\pi r\frac{\partial h}{\partial t} + \frac{\partial Q_s}{\partial r} = 0, \tag{5}$$

where h is the fan elevation and λ is the porosity of the deposit. We estimate the value of λ by comparing the volume of the deposit measured from its DEM to the volume of sediment injected into the experiment $Q_s t$. We find $\lambda = 0.4 \pm 0.02$, a common value for irregular grains.

The relation between the local slope of a river and its local sediment discharge [Eq. (4)] expresses the sediment transport along the fan:

$$\frac{B\,Q_s}{q_0 d_s} = \left(\frac{1}{A S_h}\frac{\partial h}{\partial r}\right)^{1/\alpha} - 1. \tag{6}$$

The system of Eqs. (5) and (6) is second-order in space and first-order in time. It thus requires two boundary conditions and an initial condition. The first boundary condition is set by the sediment input at the fan's apex:

$$Q_s(0,t) = Q_{s0}. \tag{7}$$

By definition, we also impose that the fan's elevation vanishes at its toe:

$$h(R,t) = 0. \tag{8}$$

As the fan grows, its radius increases and we do not know R *a priori*—the domain over which we must solve the mass balance has a free boundary. This Stefan problem thus requires an additional boundary condition. In accordance with direct observation of our experiments, we further assume that the fan traps all the sediment it is fed with. Equivalently, the sediment discharge vanishes at the fan toe:

$$Q_s(R,t) = 0. \tag{9}$$

We now seek a self-similar solution to Eqs. (5) and (6), with the associated boundary conditions, Eqs. (7), (8), and (9). We first define a similarity variable that takes into account the growth of the fan:

$$X = \frac{r}{R}, \tag{10}$$

where the radius R is a function of time which needs to be solved for. The dimensionless radius X varies between 0 and 1. Similarly, we define a dimensionless fan profile

$$H(X) = \frac{h(r,t)}{A S_h R} \tag{11}$$

and a dimensionless sediment discharge

$$\chi(X) = \frac{B\,Q_s}{q_0 d_s}. \tag{12}$$

Injecting these expressions into the sediment-transport equation [Eq. (6)] yields an ordinary differential equation:

$$H' = -(\chi + 1)^{1/\alpha}. \tag{13}$$

Next, we express the growth of the radius R as a function of the fan's shape and of the sediment input rate [Eq. (7)] based on the total sediment balance. Namely, we integrate the elevation of the fan over its domain, and differentiate the result with respect to time. We find

$$Q_{s0} = \frac{\pi}{2}\mathcal{V}(1-\lambda)\rho_s A S_h R^2 \frac{dR}{dt}, \tag{14}$$

where $\mathcal{V}$ is the dimensionless volume of the fan:

$$\mathcal{V} = 6\int_0^1 H X\, dX. \tag{15}$$

The coefficient 6 in the above definition ensure that a fan at threshold has a dimensionless volume of one. Injecting the dimensionless profile and sediment discharge [Eqs. (11) and (12)] into the mass balance equation (5) and using the radius-growth equation (14) yields another ordinary differential equation:

$$\chi' = 2\,\frac{\chi_0}{\mathcal{V}}\,X\,(XH' - H), \tag{16}$$

where χ_0 is the dimensionless sediment input:

$$\chi_0 = B\,Q_{s0}/q_0 d_s. \tag{17}$$

Finally, the two first-order, ordinary differential equations (13) and (16) need boundary conditions. In dimensionless variables, (8) and (9) become

$$\chi(1) = 0 \tag{18}$$

and

$$H(1) = 0, \tag{19}$$

respectively.

In a way, Eq. (16) is integro-differential, since it involves the dimensionless volume $\mathcal{V}$. This oddity, however, does not complicate much the numerical procedure we use to compute the self-similar profile of the fan. We simply fix the ratio $\chi_0/\mathcal{V}$ and solve Eq. (16) numerically with boundary conditions (18) and (19). We then inject the resulting profile into Eq. (15) to get

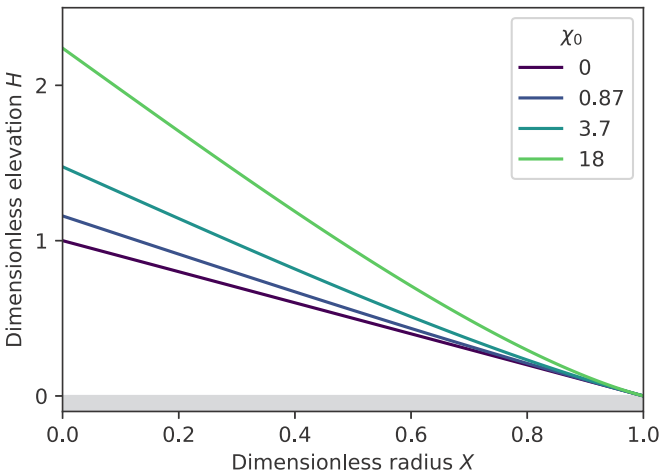

FIG. 11. Numerical fan profile for various values of the dimensionless sediment input χ_0.

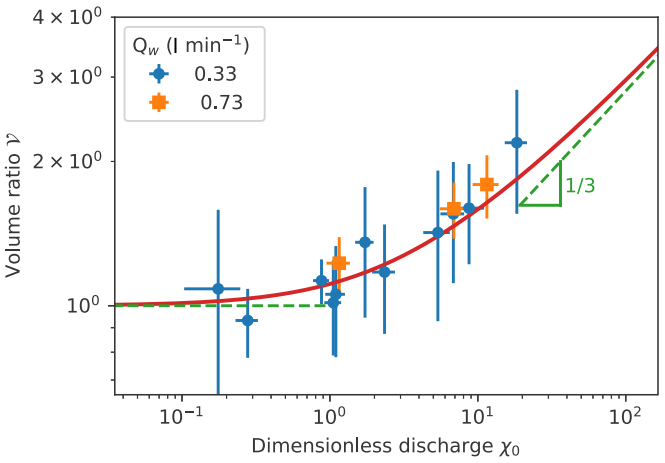

FIG. 12. Volume ratio as a function of sediment discharge. Blue and orange dots: experimental data ($Q_w = 0.33$ l min^{-1} and $Q_w = 0.73$ l min^{-1}). Red line: numerical solution. Green dashed lines: asymptotes.

the dimensionless volume and thus the dimensionless sediment input χ_0 (Fig. 11).

Like in our experiments, the numerical profiles steepen with sediment discharge. Specifically, the proximal slope increases with the sediment input rate and decreases downstream due to sediment deposition. At the fan toe, all numerical profiles merge, and the local slope reaches the threshold slope S_{th}, as expected for a vanishing sediment flux. Sediment deposition thus results in a concave upward profile.

When the sediment discharge vanishes, the entire profile converges toward the linear profile associated to near-threshold sediment transport.

In short, the slope near the fan toe is the threshold slope and therefore records the water discharge. The proximal slope, on the other hand, records the sediment discharge. In principle, we can thus use the radial profile of a fan to infer both the water and the sediment discharges that built it.

C. From morphology to discharge

The profiles of our experimental fans do not show any concavity (Fig. 9), although their dependence on sediment discharge is qualitatively similar to that of the numerical profiles. A possible cause for this discrepancy between theory and experiment is the divergence of the channel near the fan's toe (Fig. 3).

Without measurable change in slope in our experiments, we cannot infer the sediment discharge based on a local value of the fan's slope. Instead, we may use an integral quantity, likely to be less sensitive to measurement errors and natural variability. One such quantity is the fan's dimensionless volume $\mathcal{V}$, which we expect to increase with sediment discharge.

Using the numerical procedure of Sec. III B, we compute the dimensionless volume $\mathcal{V}$ for a range of dimensionless sediment discharge χ_0 (Fig. 12). The resulting curve transitions smoothly between its two asymptotes. When the sediment discharge vanishes, the fan returns to threshold, and its dimensionless volume approaches one. On the other hand, a large sediment discharge causes the fan to be so far from threshold that its slope is essentially that of its apex, which grows as the sediment discharge to the power 1/3—an unlikely regime in practice.

It is more convenient, and perhaps more telling, to express the dimensionless volume as a ratio of volumes. Specifically, $\mathcal{V}$ is the ratio of the volume of the actual fan, which we refer to as V_{fan}, to that of a hypothetical threshold fan with the same radius:

$$\mathcal{V} = \frac{6\, V_{\text{fan}}}{(1-\lambda)\pi\, A S_h R^3}. \tag{20}$$

For illustration, we measure the volume of our laboratory fans using their DEMs. We then calculate their volume ratio $\mathcal{V}$ according to the above formula and their dimensionless discharge χ_0 according to Eq. (17). Plotting these quantities in Fig. 12, we find that our experimental data accord reasonably with the self-similar theory of Sec. III B.

IV. CONCLUSION

Using a simplified setup, we produced fans fed by a single-thread river, which controls their slope, while avulsions maintain their radial symmetry. The growth of the fan is self-similar, and its radius grows like time to the power 1/3. To assess the influence of the fluid and sediment discharges on the fan profile, we combine these laboratory observations with a first-order theoretical analysis.

For a low sediment discharge, the threshold of sediment motion controls the slope of our experimental fans, as it controlled the one-dimensional alluvial fan produced by Guerit *et al.* [22]. When the sediment discharge increases, so does the fan slope, especially near the fan apex, where the sediment discharge is the highest. As a consequence, the fan profile exhibits a slight curvature [22].

According to the semiempirical theory presented here, the slope near the fan's toe is an indicator of fluid discharge. Similarly, the ratio of apex slope to toe slope is a proxy for sediment discharge. In this simplified framework, we can thus use the present shape of an alluvial fan to infer the paleofluxes that built it.

Before applying this theory to field observations, however, we will need to adapt it. First, the sediment discharge does not always vanish at the toe of a fan [36–38]. Consequently, we cannot use the distal slope as a straightforward proxy for water discharge; we first need to evaluate the sediment discharge that exits the fan. Given this measurement, we can probably extend the present theory to this new boundary condition.

In nature, alluvial fans are made of heterogeneous sediments. The river that transports them also sorts them according to mobility [28,39]. The coarser sediment gets deposited near the apex, whereas the finer one ends up at the toe or even exits the fan. This segregation causes the fan slope to decrease downstream [40]. Thus, both deposition and downstream fining translate into a concave upwards profile. To isolate these processes, we need reliable transport laws and a mass balance that can handle a distribution of grain sizes [12,28].

Sediment and water inputs are likely to vary during the fan history. If so, the self-similar theory presented here does not hold, as the shape of the deposit surface can record only the last increment of growth. However, the river probably adjusts its profile to varying conditions quickly—at least with respect to the fan's growth. If this is indeed true, the transport law and the mass-balance equation would still hold, and we could solve them numerically to follow varying inputs.

Finally, the sediment deposited at a specific period is often recognizable in the internal structure of the fan, in the form of a stratum. Interpreting these strata as proxies for paleoprofiles, geologists can reconstruct the shape of ancient fans [41,42]. Using these paleoprofiles as we have used the DEMs of our experiments, we might infer ancient mass fluxes and the tectonic and climatic forcings that induced them.

ACKNOWLEDGMENTS

We thank R. Vasquez, H. Bouquerel, and A. Limare for their help in building the experimental setup, E. Gayer for his help with DEM processing, and E. Lajeunesse, C. Paola, and V. Voller for fruitful discussions. O.D. was partially funded by the Émergence(s) program of the Mairie de Paris, France.

[1] W. B. Bull, Progress Phys. Geog. **1**, 222 (1977).
[2] A. Rachocki and M. A. Church, *Alluvial Fans: A Field Approach* (John Wiley & Sons, New York, 1990).
[3] T. C. Blair and J. G. McPherson, J. Sediment. Res. **64**, 450 (1994).
[4] A. M. Harvey, A. E. Mather, and M. Stokes, Geol. Soc. Lond. Spec. Publ. **251**, 1 (2005).
[5] T. C. Blair and J. G. McPherson, in *Geomorphology of Desert Environments* (Springer, New York, 2009), pp. 413–467.
[6] J. Field, Geomorphology **37**, 93 (2001).
[7] R. Slingerland and N. D. Smith, Annu. Rev. Earth Planet. Sci. **32**, 257 (2004).
[8] R. Sinha, Curr. Sci. **97**, 429 (2009).
[9] F. Drew, Q. J. Geol. Soc. **29**, 441 (1873).
[10] E. Blissenbach, J. Sediment. Res. **22**, 25 (1952).
[11] C. S. Denny, *Alluvial Fans in the Death Valley Region, California and Nevada*, Geological survey professional paper 466 (US Government Printing Office, Washington, DC, 1965).
[12] J. D. Stock, K. M. Schmidt, and D. M. Miller, Geol. Soc. Am. Bull. **120**, 619 (2008).
[13] S. A. Schumm, M. P. Mosley, and W. Weaver, *Experimental Fluvial Geomorphology* (John Wiley and Sons, New York, 1987).
[14] G. Parker, J. Hydraul. Res. **37**, 805 (1999).
[15] C. Paola, K. Straub, D. Mohrig, and L. Reinhardt, Earth-Sci. Rev. **97**, 1 (2009).
[16] L. E. Clarke, Geomorphology **244**, 135 (2015).
[17] K. X. Whipple, G. Parker, C. Paola, and D. Mohrig, J. Geol. **106**, 677 (1998).
[18] G. Parker, C. Paola, K. X. Whipple, D. Mohrig, C. M. Toro-Escobar, M. Halverson, and T. W. Skoglund, J. Hydraul. Eng. **124**, 996 (1998).
[19] M. Van Dijk, G. Postma, and M. G. Kleinhans, Sedimentology **56**, 1569 (2009).
[20] L. Clarke, T. A. Quine, and A. Nicholas, Geomorphology **115**, 278 (2010).
[21] E. J. Powell, W. Kim, and T. Muto, J. Geophys. Res.: Earth Surf. (2003–2012) **117**, 1 (2012).
[22] L. Guerit, F. Métivier, O. Devauchelle, E. Lajeunesse, and L. Barrier, Phys. Rev. E **90**, 022203 (2014).
[23] G. Lacey, in *Minutes of the Proceedings of the Institution of Civil Engineers*, Vol. 229 (Thomas Telford-ICE Virtual Library, London, 1930), pp. 259–292.
[24] M. D. Reitz and D. J. Jerolmack, J. Geophys. Res.: Earth Surf. (2003–2012) **117**, 2 (2012).
[25] G. Seizilles, O. Devauchelle, E. Lajeunesse, and F. Métivier, Phys. Rev. E **87**, 052204 (2013).
[26] A. Shields, Preussische Versuchsanstalt Wasserbau Schiffbau **26**, 524 (1936).
[27] G. Seizilles, E. Lajeunesse, O. Devauchelle, and M. Bak, Phys. Fluids (1994–present) **26**, 013302 (2014).
[28] P. Delorme, V. Voller, C. Paola, O. Devauchelle, E. Lajeunesse, L. Barrier, and F. Métivier, Earth Surf. Dyn. **5**, 239 (2017).
[29] J. H. Bruning, D. R. Herriott, J. Gallagher, D. Rosenfeld, A. White, and D. Brangaccio, Appl. Opt. **13**, 2693 (1974).
[30] F. Brémand, Optics Lasers Eng. **21**, 49 (1994).
[31] A. Limare, M. Tal, M. Reitz, E. Lajeunesse, and F. Métivier, Solid Earth **2**, 143 (2011).
[32] R. E. Glover and Q. Florey, *Stable Channel Profiles* (US Department of the Interior, Bureau of Reclamation, Hydr. Lab. Report, Washington, DC, 1951).
[33] F. M. Henderson, J. Hydraul. Div. **87**, 109 (1961).
[34] F. Charru, H. Mouilleron, and O. Eiff, J. Fluid Mech. **519**, 55 (2004).
[35] G. Parker, C. Paola, K. X. Whipple, and D. Mohrig, J. Hydraul. Eng. **124**, 985 (1998).
[36] E. Kiefer, M. J. Dorr, H. Ibbeken, and H.-J. Gotze, Andean Geol. **24**, 165 (1997).

[37] T. Oguchi, J. Quaternary Sci. **12**, 381 (1997).
[38] M. Jolivet, L. Barrier, S. Dominguez, L. Guerit, G. Heilbronn, and B. Fu, Geomorphology **214**, 168 (2014).
[39] K. L. Miller, M. D. Reitz, and D. J. Jerolmack, Geophys. Res. Lett. **41**, 7191 (2014).
[40] W. B. Bull, *Geomorphology of Segmented Alluvial Fans in Western Fresno County, California* (US Government Printing Office, Washington, DC, 1964).
[41] J. Hornung, D. Pflanz, A. Hechler, A. Beer, M. Hinderer, M. Maisch, and U. Bieg, Geomorphology **115**, 202 (2010).
[42] S. Rohais, S. Bonnet, and R. Eschard, Basin Res. **24**, 198 (2012).